

An Alternative Beam Alignment Approach for Tactical Systems

Dan Herrick

Optics Division, AFRL/DES, Directed Energy Directorate
U.S. Air Force Research Laboratory, Kirtland AFB, NM 87117-5776 USA

Pawel K. Orzechowski, Steve Gibson and Tsu-Chin Tsao

Mechanical and Aerospace Engineering
University of California, Los Angeles 90095-1597 USA

Milind Mahajan and Bing Wen

Teledyne Scientific Company
1049 Camino Dos Rios, Thousand Oaks, CA 91360 USA

ABSTRACT

Optical line of sight stability of a high energy laser weapon is maintained by employing a high bandwidth jitter control system. This controller needs a “clean” measure of beam train line of sight jitter. This is usually accomplished by inserting a stabilized laser beam that passes over most mirrors in the optical train. The stabilization of this beam is accomplished by mounting a small fiber fed collimator on an inertially stabilized platform. Functionally these devices look a bit like a fast steering mirror with gyros and optics attached to the “mirror” surface. For tactical systems which have small apertures, packaging becomes critical and allowable jitter levels are relatively large. For this case a compact approach is proposed where no mechanical stabilization is attempted. A transmissive liquid crystal beam dithering device is mounted in front of the collimator. The rotational motion of the collimator is measured and fed forward to a beam dithering device to stabilize the emerging alignment beam. This approach is enabled by calibrating the feedforward filter using adaptive techniques. This presentation describes the liquid crystal beam dithering device, the adaptive feedforward filtering and laboratory experiments which assess the performance limits of such an approach.

Keywords: Adaptive control, laser-beam steering, jitter, liquid crystal beam steering device

1. INTRODUCTION

This is a progress report of research into internal optical train jitter rejection for a new class of tactical HEL weapons. Tactical HEL weapons that are presently being considered are diminutive compared with systems like the Advanced Tactical Laser (ATL) or Airborne Laser (ABL). This new class of weapon has an output aperture of 30 cm and weighs only several thousand pounds. Great effort is being exerted to miniaturize and simplify all aspects of beam control systems of these devices. Line of sight stability requirements scale with aperture diameter so jitter stabilization isn’t as demanding as on ABL or ATL. On the other hand these small tactical weapons are likely to be put in less benign disturbance environments, for instance in an under wing pod. Internal line of sight stabilization is most likely still going to be required.

Figure 1 shows the range of architectural possibilities for the jitter stabilization system. These are schematic notions representing the high power optical train from the target to the beam expander and down to the tracker focal plane. If the target is bright enough for a high signal to noise ratio image on the tracking focal plane then a high bandwidth track loop (Fig. 1: top left) may suffice to stabilize the line of sight. This is unlikely

E-mail: pawel.orzechowski@yahoo.com, gibson@ucla.edu, ttsao@ucla.edu, dancherrick@comcast.net, mmahajan@teledyne.com, bwen@teledyne.com

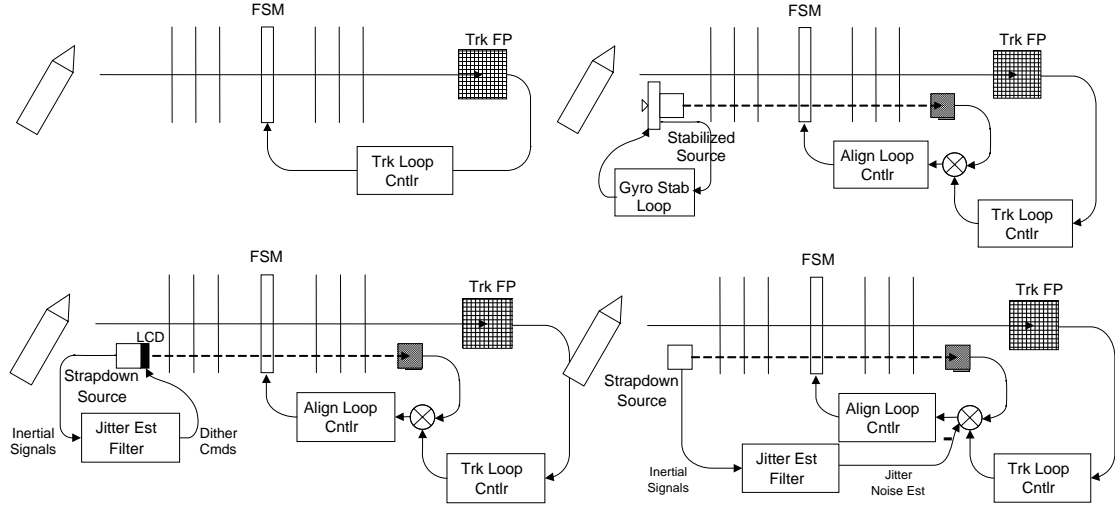


Figure 1. Tactical line of sight stabilization options. Top left: using image track errors; top right: using inertially stabilized alignment beam; bottom left: Using strap down stabilized alignment beam; bottom right: using alignment beam noise cancellation.

since it is always desirable to extend the target space to dimmer objects. Also the bandwidth required to reject atmospheric tilt jitter is likely to be less than the bandwidth required to reject internal optical train jitter. This leads to the desire to have separate track and line of sight stabilization loops. This leads to the standard solution of adding an internal alignment beam (Fig. 1: top right). This is inserted into the optical train at the primary mirror of the beam expander. This beam, coming from output space, samples all of the high power optics down to the tracker focal plane. This device has been called a pseudo-star which provides a high signal to noise ratio spot that appears in the target direction. A high bandwidth stabilization loop can be closed on this pseudo-star to reject internal jitter.

An appropriate bandwidth track loop can be independently closed that balances atmospheric tilt disturbance rejection and track noise insertion. The stabilized source for this approach is a technological marvel akin to a stabilized inertial platform. Rotation rate sensors capable of low noise, high bandwidth measurements are mounted on flexure suspended base. The platform is driven by voice coil actuators. These rate sensors are usually combined instruments, a gyro and high frequency, low noise device. Such an instrument allows high bandwidth rate stabilization of the platform. A laser diode source is fed through a fiber to a collimator mounted on the stabilized platform. Since the platform has a dc attitude reference it can be driven to a target vector coordinate with the beam expander telescope in a servo following mode. These stabilized source devices are shrinking and can be simplified by eliminating the dc gyro if the target queuing function is done some other way.

The instrument of interest in this research (Fig. 1: bottom left) eliminates the suspended platform and has no moving parts. It consists of a fiber fed collimator, inertial instruments to sense the unit rotation, a transmissive liquid crystal (LC) tilt corrector and an adaptively tuned filter. The adaptive filter takes inputs from the inertial rotation instruments and outputs tilt corrector commands. The inertial instruments have no dc response. Therefore the strap-down beam source has no attitude reference and cannot be used to queue the beam expander to target coordinates.

The adaptive filter tuning will be done during instrument integration but could be re-accomplished in-situ when the weapon system is tracking a high signal to noise ratio calibration target. Since the strap-down instrument is simpler, having fewer components and no moving parts, it should ultimately be smaller and lighter than the stable platform. The efforts to work through the significant performance issues of the strap-down approach are described in this paper. One might ask whether the alignment beam needs to be stabilized at its source (Fig. 1: bottom right). The instrument jitter information used to command the tilt corrector could be

used to cancel this beam noise from the error signal driving the alignment loop. This is an alternative which will be examined in the later stages of this research. The ultimate choice between stabilizing the alignment beam or removing this noise from the servo error signal may be determined by beam control architectural considerations.

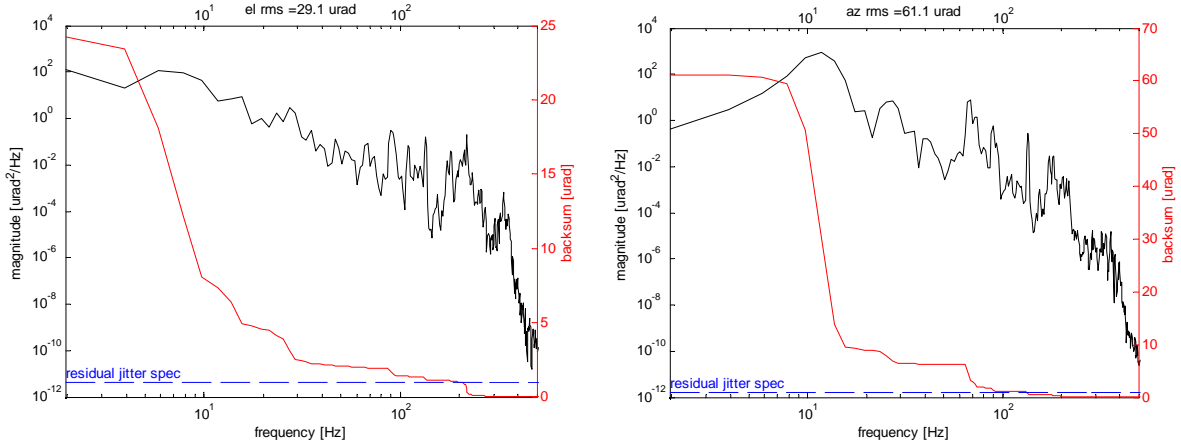


Figure 2. Base rotation spectra in prototypical tactical beam expander.

The notional jitter environment for this instrument is shown in Fig. 2. This is taken from a structural model of a prototypical airborne beam pointer. The important features of these base motion rotational spectra are magnitude, 10's of μrad , and bandwidth out to 100 Hz. This represents a hard mounting point and these levels could be reduced by soft mounting the alignment beam device. These jitter spectra drove the performance requirements of the liquid crystal tilt corrector described below.

We are employing a phased approach to demonstrate this instrument concept. The driving performance issue is to determine in a practical sense the degree of line of sight jitter rejection achievable by feed forward adaptive filtering. This limit will be determined by the servo characteristics of the inertial instruments and the LC tilt corrector and the ability of the adaptive filter to integrate these two components. Measuring this performance does not require the complete integration of a two axis instrument. The two axis demonstration will be done in a final demonstration test. In fact for preliminary testing the mechanical design issues can be avoided by pulling the instrument apart. A one axis vibration test fixture (Fig. 3: top right) includes just the inertial instruments tightly attached to a dove prism. This is mounted on a cantilevered plate with a shaker. Mounted on a separate stable table are an alignment laser, the LC tilt corrector and a PSD sensor. The alignment beam is reflected through the dove prism, back through the LC tilt correcting device and onto the PSD. The PSD sensor is not part of the instrument package. Its output is used to train the adaptive filter. The inertial sensors and the beam jitter are very coherent as they would be in a properly designed instrument but the laser source and LC tilt corrector are not subjected to the mechanical disturbance. This approach lets us deal with critical servo issues uncomplicated by possible mechanical design issues.

The prototype instrument fixture (Fig. 3: top left) is being tested separately. This hardware includes the laser diode source, fiber fed to a collimating telescope and the attachment for the LC tilt corrector. This fixture will be tested on the vibration bench at Starfire Optical Range Jitter Lab (Fig. 3: bottom). These tests will characterize extraneous beam jitter introduced by the fiber coupling and vibration modes the fixture. This will be a major contributor to the instrument's stabilization noise floor. The prototype instrument has an 8 inch base which is much larger than an actual flight instrument. This approach was taken to avoid ticklish design and integration issues but still demonstrate a fully integrated instrument. The integrated two axis instrument will be tested on the large vibration bench and its beam stabilization performance limits determined.

The LC tilt corrector is described in Section 2. Preliminary experiments at UCLA investigate servo characteristics and performance limits of the LC tilt corrector in a closed loop control system which are described in Sections 3–5.

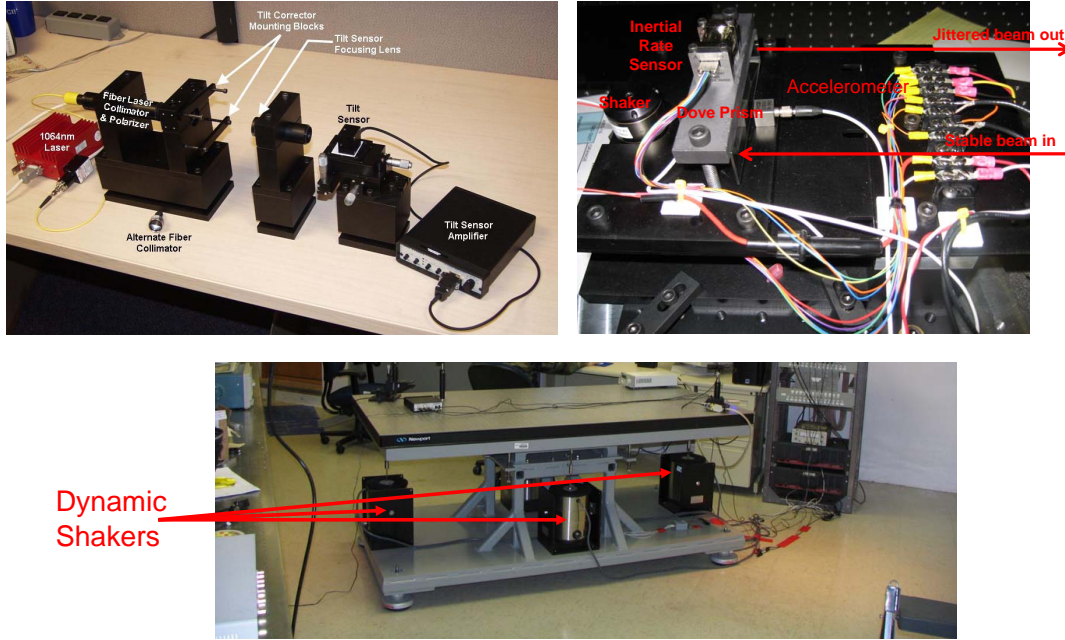


Figure 3. AFRL beam steering experiment. Top left: Two axis proof of concept strapdown alignment source; top right: single axis beam motion fixture with inertial instruments; bottom: two axis jitter bench platform used for instrument testing.

2. TRANSMISSIVE LIQUID CRYSTAL TILT CORRECTOR

2.1. Tilt Corrector Performance Description and Trade-offs

The transmissive liquid crystal tilt corrector was developed by Teledyne Scientific Company (TSC) in Thousand Oaks, CA. The liquid crystal tip-tilt corrector leverages dual frequency liquid crystal optical phased array (OPA) technology¹ to address the need for a compact, transmissive, high-speed tip-tilt correction device in a laser electro-optic system. The primary difference between optical phased arrays and the tilt corrector is that tip-tilt corrector does not have phase resets across the aperture. The tip-tilt corrector architecture does not suffer from amplitude modulation as the beam is steered across the field-of-regard (FOR), which is an issue for OPA. Additionally, it provides improved diffraction efficiency and significantly higher angle update rate compared to an OPA. This architecture is generally limited to a FOR that is smaller than a device employing modulo- 2π phase resets.

Our 2 cm aperture transmissive tip-tilt corrector has $\pm 300 \mu\text{rad}$ FOR in both dimensions, $2 \mu\text{rad}$ steering resolution, 3.125 kHz frame rate, and 24 mrad/s slew rate. This design offers fundamental advantages over a fast steering mirror of similar aperture and bandwidth:

1. No moving parts, which increases tilt corrector durability and eliminates the need for reaction compensation
2. Transmissive architecture, which significantly reduces coupling of platform and acoustic disturbances
3. Lithographic fabrication and simple assembly process, which significantly reduce recurring costs
4. Absolute phase control, which eliminates the need for costly position feedback sensors and lowers power dissipation
5. Low voltage operation, which significantly reduces controller size, weight and power

The tilt corrector design uses proprietary TransconTM low-loss transparent conductor films, which has an absorption of 0.2–0.3% (depending on sheet resistance) at 1 micron wavelength. An optimized design is expected

to result in $\sim 89\%$ efficiency ($\sim 4\%$ diffractive loss, 2.6% absorption, 3.6% scattering and $\sim 1\%$ Fresnel loss). The current device has 70% efficiency ($\sim 4\%$ diffractive loss, $\sim 3\%$ absorption, $\sim 10\%$ Fresnel loss and $\sim 17\%$ loss due to undesirably large gaps between pixels). The difference can be explained by additional losses incurred from the use of unoptimized TransconTM layer with no anti-reflection coating and large gap between the pixels due to excessive etching time. Both factors can be corrected in future devices.

Each liquid crystal cell used in the tip-tilt corrector has twenty 2-cm long 1-mm wide pixels on one side of $15\text{ }\mu\text{m}$ thick liquid crystal layer and a single ground plane on the other. Each pixel can be used as a phase modulator where absolute phase control is possible by application of corresponding voltage. Steering is achieved by applying a staircase like phase ramp across the aperture. Transition from one deflection to another involves changing phase on several pixels.

TSC uses dual frequency liquid crystals (DFLCs)^{2,3} for high-speed steering applications in the near infrared because this class of materials surpasses all others in terms of switching speed, phase stability and electronic controller size, weight and power. The control voltages are applied at two frequencies ($f_L \sim 3.125\text{ kHz}$ and $f_H \sim 100\text{ kHz}$). Voltages up to 20 volt RMS are applied to accelerate the phase transition (“kicking voltage”), while voltages between 2 and 6.5 volt RMS (4.5 volt range) are applied to maintain a given phase level (“holding voltage”). The kicking duration is $320\text{ }\mu\text{s}$ or 1 frame and the holding duration is $640\text{ }\mu\text{s}$ or 2 frames. The holding duration allows any residual settling and prevents phase errors from building up over long duration. The kicking waveforms are staggered across the three cells such that in any given frame one of the three cells per steering dimension is being updated with a new angle.

DFLC beam steering devices including tilt corrector have an upper limit on slew rate. Two ways to improve the slew rate are increased kicking voltage (up to a limit determined by onset of flow instability in liquid crystals) and reduced thickness. We used the entire voltage throw available through the 20 volts multi-chip dual frequency liquid crystal drive modules. We reduced thickness using three thinner liquid crystal cells per steering dimension instead of one thick cell. Thus the particular variation of the architecture implemented in the current design consists of six identical cells, three per dimension, each capable of steering over $\pm 100\text{ }\mu\text{rad}$ steering range.

2.2. Tilt Corrector Component Description

The physical implementation of the tilt corrector is shown in Fig. 4. The six liquid crystal cells are fabricated using twelve substrates (each $\sim 0.5\text{ mm}$ thick) and laminated together using an index matching gel. In the six-cell stack, the first three cells have liquid crystal oriented along the pixels. The remaining three cells have the liquid crystal oriented perpendicular to the pixel length and their pixels are perpendicular to those of first three in the laminated stack. This allows an X-Y steering geometry without using a polarization rotator between the X and Y stacks. Thick substrates of $\sim \lambda/20$ surface figure with outside surface AR coated are laminated to the outer cells on either side to maintain good transmitted wavefront. The number of control channels required to steer one polarization in one dimension is 60 (three 20-pixel cells). Consequently, 120 control channels, or three 40-channel multi-chip controller modules (MCMs), are required to steer one polarization in two dimensions. The 40-channel MCM uses a 12-bit digital-to-analog converter (DAC) that has an effective resolution of 11 bits over a 20-volt range. The voltage increment of the controller is therefore 5 mV, with a voltage precision of 10 mV. The DFCLC phase-voltage relationship is approximately sigmoidal in shape, and the steepest portion of the curve will therefore have a phase precision of $\lambda/100$. We fabricated a 160-channel driver using four 40-channel multi-chip dual frequency drive modules that can accept new voltage and frequency data at 3.125 kHz frame rate over a 16 bit parallel digital bus. Figure 5 shows the photograph of tilt corrector optical head, 160-channel DFCLC driver and Blackfin 537 based stand alone controller.

2.3. Device Calibration

Precise calibration procedure is required to operate the tilt corrector at high refresh rate. The calibration begins with measurement of the phase-voltage relationship of each liquid crystal cell. The ambient temperature is maintained at $52 \pm 1\text{ }^\circ\text{C}$. The middle $2\text{ }\mu\text{m}$ wide portion of available phase throw is divided into 50 discrete phase levels. The next step involves measuring precise voltage amplitudes required for a transition from one phase level to another in one frame ($320\text{ }\mu\text{s}$ duration). The available voltage allows transition through ± 4 phase levels in one frame. Several kick-ing voltages are manually optimized by kicking the device back and forth between

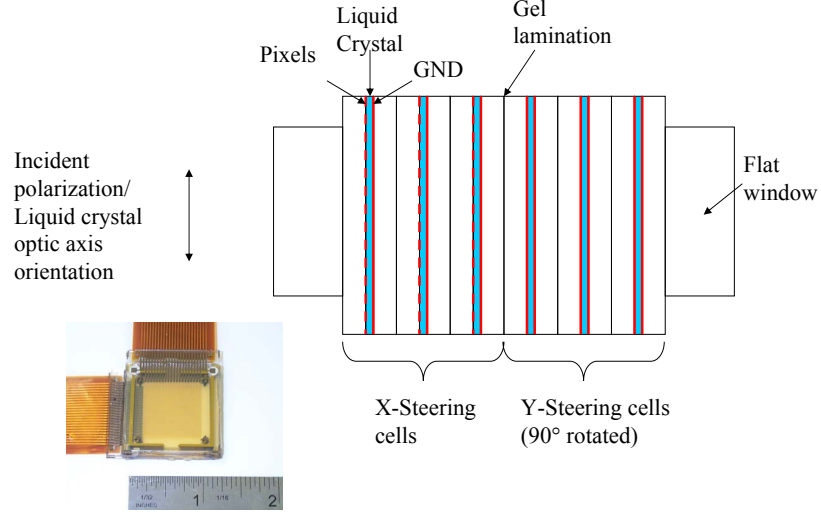


Figure 4. Physical structure of a six cell tilt corrector. The photograph show a flex connectorized 6-cell stack without front and back windows

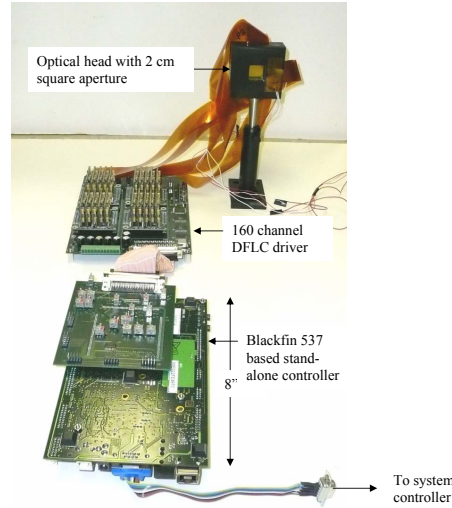


Figure 5. Liquid crystal tilt corrector packaged optical head, 160 channel DFLC driver, and stand-alone controller

the desired phase levels and by measuring the optical response between crossed polarizers. The optimal kicking voltage V_{k12} , to go from phase-level 1 to phase-level 2 with the corresponding voltages V_1 and V_2 , is given by

$$V_{k12} = A_{12} \sqrt{\frac{V_2 - V_1}{V_2 + V_1 - V_{th}}}, \quad (1)$$

where A_{12} and V_{th} are the parameters to be determined from fit to experimental data. The expression is then used to calculate kicking voltage for transition from any phase level to any other phase levels. We divided the $200 \mu\text{rad}$ steering range of each cell into 100 angular steps (separated by $2 \mu\text{rad}$) and calculated the staircase like phase profile required for each of these angle positions.

TSC developed a stand-alone controller based on a Blackfin 537 processor. It stores the calibration data that includes phase profiles corresponding to 100 angular positions, voltages corresponding to 50 phase levels per cell, fit coefficients describing the kicking behavior of the cells. The controller accepts on 8-bit parallel digital control

signal that commands the controller to increase or decrease the current deflection along X and Y-direction by a certain angle (up to 8 μrad , in steps of 2 μrad). The controller then selects the appropriate cell that is ready to accept an angle update and commands it to go to a new deflection using appropriate calibration data. It generates the 16-bit command and sends it to the 160-channel driver. It also returns a digital timing output to synchronize the system controller with the tilt corrector driver. This controller eliminates the need for the end users to understand dual frequency liquid crystal physics and the low level programming of 160-channel driver allowing a user-friendly high-level control.

Figure 6 shows the oscilloscope traces of vertical and horizontal deflection of the beam as measured by a duolateral detector when this system continuously scans the beam (open loop) across its FOR at 24 mrad/s. The peak-to-peak angular deflection of 600 μrad is scanned in ~ 25 ms.

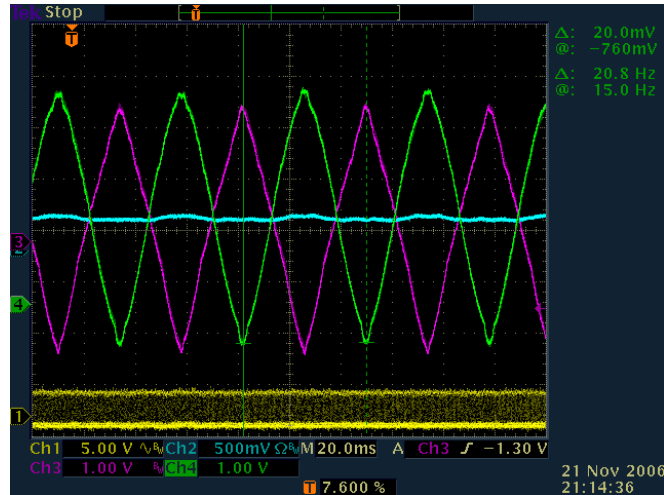


Figure 6. Figure shows the oscilloscope traces of vertical and horizontal deflection of the beam as measured by a duolateral detector when the device continuously scans across its FOR at 24 mrad/s. The peak-to-peak angular deflection of 600 μrad is scanned at ~ 25 ms.

2.4. Future Improvements

1.5X improvement in the top slew rate of the device (from 24 mrad/s to 36 mrad/s) is possible by using one frame kick and one frame hold on the cells instead of current one frame kick and two frame hold scheme. If the temperature stabilization (currently at ± 1 $^{\circ}\text{C}$) window is improved by better thermal design, hold time can be further shortened and the slew rate boosted to 48 mrad/s. Faster slew rate will enable the device to correct faster disturbances. Elimination of lithographic defects and optimization of TransconTM for 1 μm wavelength (including AR coating or index matching of TransconTM layer) will further improve optical efficiency. Lithographic imperfections can also be easily eliminated. The next revision could use an increased switching voltage throw, which could be used to enable higher slew rate, higher steering range or a reduced number of cell count. Next generation of DFLC driver is expected to have double the kicking voltage along with significant reduction in size. There is also a possibility of using more complex architectures such as monolithic phased array of phased arrays to further reduce the channel count.

3. EXPERIMENTAL SETUP

The optical components of the beam steering experiment, shown in Figs. 7 and 8, are a 980nm laser, a wire grid linear polarizer, the liquid crystal beam steering device, a fast steering mirror (FSM) mounted on top of a shaker, a rigid folding mirror, a convergent lens, followed by another rigid folding mirror and an optical position sensor (OPS) that tracks the position of the image that the laser beam forms on the plane of the sensor. The

two dimensional vector y denotes the measured position of the laser spot. The steering mirror labeled FSM and the shaker are used as additional jitter sources. The control, measurement, and disturbance command sequences are processed in real-time using MATLAB's xPC Target real-time software on a 3.6 GHz Pentium operating at a sample-and-hold rate, governed by the liquid crystal device's driver electronics, of approximately 3125 Hz.

There are three independent sources of jitter, denoted by d_B , d_C , d_S in Fig. 7. The misalignments and the unintentional vibration of the optical components are due to the building vibration, denoted by d_B . The disturbance mirror FSM is driven by the disturbance command sequence d_C and the shaker is driven by the disturbance sequence d_S . Both d_S and d_C are produced by passing white noise sequences through stable band-pass filters designed to produce desired jitter bandwidths, which are described in Section 5. The two dimensional vector v denotes the final control sequence sent to the liquid crystal device.

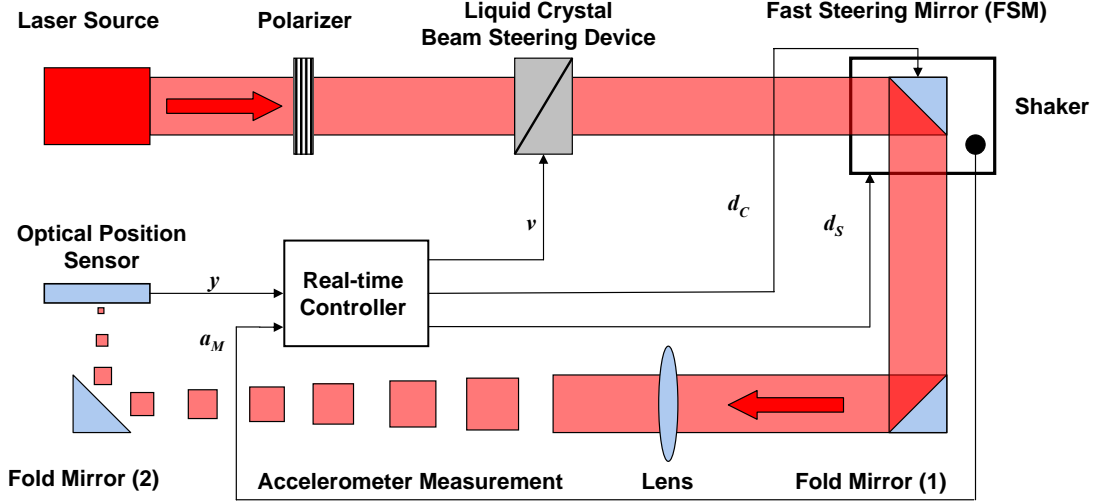


Figure 7. Diagram of the experiment.

4. ADAPTIVE CONTROL

4.1. Model of the Liquid Crystal Beam Steering Device

The electronic driver of the liquid crystal beam steering device receives incremental commands at a 3125 Hz rate. This slew rate command has a specified allowable range. The device is able to steer the beam to a finite number of quantized states, which cover beam deflection angle range of $\pm 300 \mu\text{rad}$. While the device's state transition occurs rapidly within the update rate of 3125 Hz, the quantization, angle, and slew rate saturation pose limits on resolution and dynamic response, which cannot be simply characterized by linear filter and bandwidth. Figure 9 shows the block diagram of the device under a feedback control loop. The input to the device is the vector v and the output of the device is the vector θ . The saturation blocks in Fig. 9 are characterized by the following for each axis ($i = 1, 2$):

$$\text{Rate Limit Output} = \begin{cases} v_i, & \text{if } |v_i| \leq 4 \\ 4, & \text{if } v_i > 4 \\ -4, & \text{if } v_i < -4 \end{cases}, \quad (2)$$

$$\text{Angle Saturation Output} = \begin{cases} \phi_i, & \text{if } |\phi_i| \leq 150 \\ 150, & \text{if } \phi_i > 150 \\ -150, & \text{if } \phi_i < -150 \end{cases}, \quad (3)$$

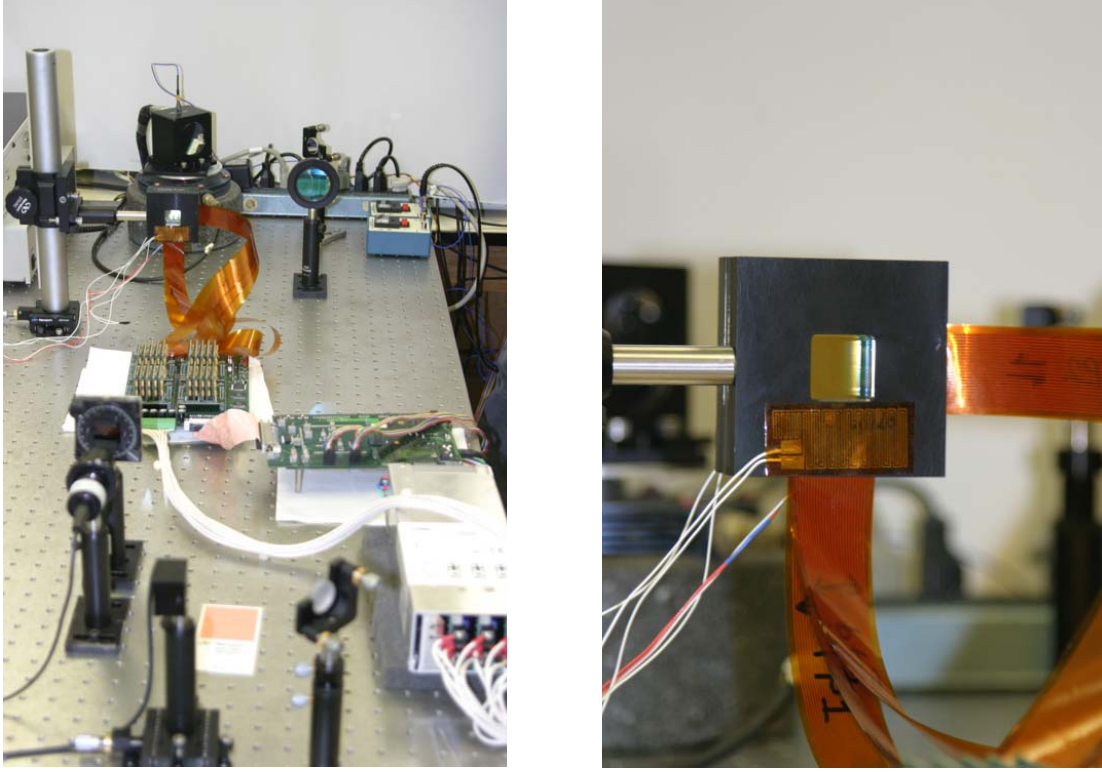


Figure 8. UCLA laser beam steering experiment. Left: the liquid crystal beam steering experiment. Right: zoomed-in picture of Teledyne's liquid crystal beam steering device.

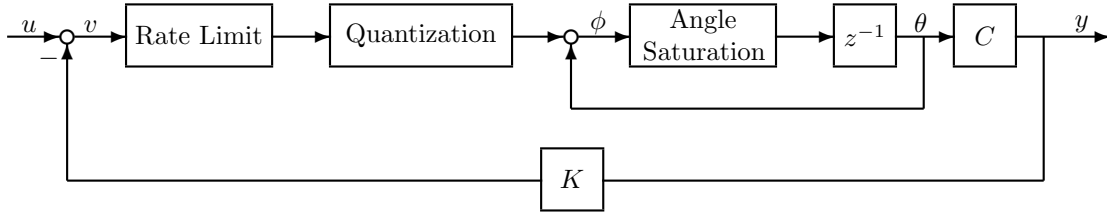


Figure 9. Block diagram of the liquid crystal device and LTI feedback control loop. The signals (all two-dimensional): y = measurement vector from optical position sensor, θ = beam angle vector, v = net control command before saturation and quantization, u = feedforward adaptive control command. Constant matrices: K = diagonal feedback control gain, C = diagonal matrix of conversions factors.

and the block labeled quantization, rounds the input to the nearest integer value. The entries in the vectors ϕ and θ take on integer values, where each integer value corresponds to a $2 \mu\text{rad}$ angular beam displacement. The gain matrix C converts the beam angles θ to the position measurements y , given by the optical position sensor (OPS). The mapping from the adaptive control command vector u to the output position error y is denoted by G . The experimental results confirm G is essentially diagonal; i.e., steering the beam with the liquid crystal beam steering device in one direction has negligible effect on the motion of the beam in the other direction. Hence G is modeled as diagonal, and the matrix C that converts angular beam displacement to linear displacement on the sensor is

$$C = \begin{bmatrix} c_1 & 0 \\ 0 & c_2 \end{bmatrix} = \begin{bmatrix} 0.01677 & 0 \\ 0 & 0.01515 \end{bmatrix}. \quad (4)$$

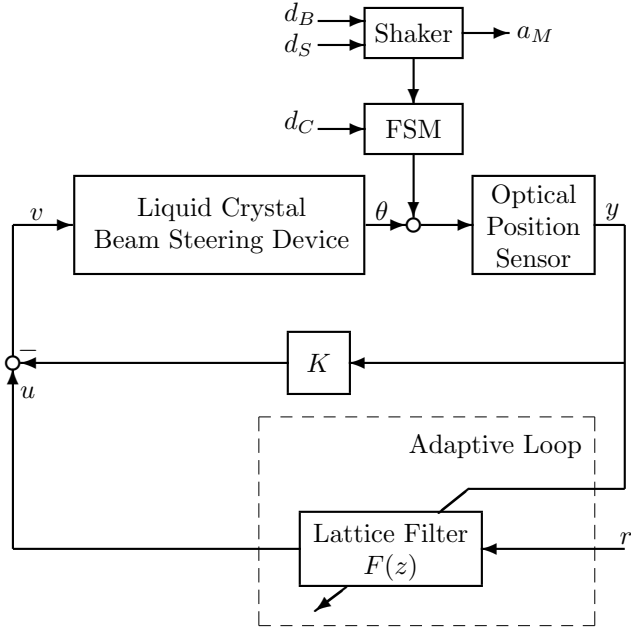


Figure 10. Block diagram of the control system. d_S = disturbance command to shaker; d_B = building vibration; d_C = disturbance command to FSM; d_M = response of FSM; θ = beam angle from liquid crystal beam steering device; y = beam position on sensor; r = reference signal for feedforward adaptive control; u and v = control commands.

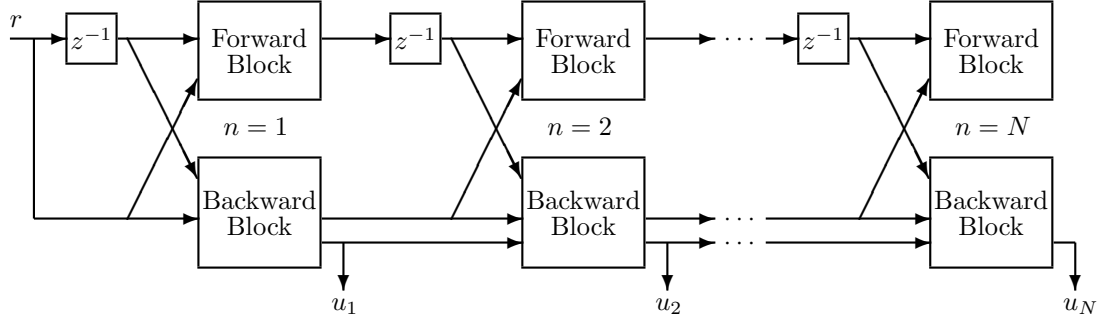


Figure 11. The FIR lattice filter generates adaptive control commands u_n for all filter orders $n \leq N$.

To determine the values of c_1 and c_2 , the liquid crystal beam steering device and the model in Fig. 9 were driven with an open-loop white-noise sequence v (without the control loops closed). The resulting output sequences were used to compute the values of c_1 and c_2 to produce the least-squares fit between experimental and simulated output sequences.

The feedback gain matrix K was chosen to be

$$K = \begin{bmatrix} k_1 & 0 \\ 0 & k_2 \end{bmatrix} = \begin{bmatrix} 2 & 0 \\ 0 & 2 \end{bmatrix}. \quad (5)$$

The feedback gains in K were chosen to maximize the error-rejection bandwidth with minimal amplification of high-frequency disturbance. Attempting to increase the bandwidth by increasing the gain K would produce greater amplification of high-frequency disturbance.

4.2. Adaptive Control Loop

When the LTI feedback control loop is closed (see Fig. 10), it is assumed there exist stable LTI transfer function G , G^{yC} , G^{yS} and G^{yB} such that

$$y = Gu + w, \quad (6)$$

where

$$w = G^{yS}d_S + G^{yB}d_B + G^{yC}d_C, \quad (7)$$

The output disturbance w represents the combined effect of the jitter signals from the shaker, the building vibration and the disturbance mirror FSM, filtered through the appropriate closed-loop transfer functions. Any sensor noise associated with the optical position sensor would be added to the right side of (7); however, careful measurements of the output of the OPS have shown that any sensor noise is negligible in the experiments reported here.

The main component of the adaptive controller is the RLS lattice filter $F(z)$. For this paper, the input (or reference signal) to $F(z)$ is r , which is shown in Fig. 10. The lattice filter can use an arbitrary number of inputs for generating the command for each control channel. The adaptive control methods presented in this paper use only a single input measurement for the reference signal r .

The lattice filter implicitly tracks the statistics of the disturbance and identifies gains to minimize approximately the RMS value of the output error signal y . The precise least-squares criterion minimized by the lattice filter is the RMS value of sequence $\hat{w} + F\hat{G}r$. The sequence \hat{w} is given by

$$\hat{w} = y - \hat{G}u. \quad (8)$$

Since \hat{G} is a scalar transfer function for each of the uncoupled control channels,

$$\hat{w} + F\hat{G}r = \hat{w} + \hat{G}Fr. \quad (9)$$

Therefore, if $\hat{G} = G$,

$$\hat{w} + F\hat{G}r = \hat{w} + \hat{G}Fr = w + GFr = y. \quad (10)$$

The adaptive controller can reject biases in the disturbance. However, since the LTI feedback loop rejects any biases, the output signal y has zero mean throughout this paper because the classical track loop is always closed. Therefore, the RMS value and standard deviation of y are the same in steady-state.

Adaptive control schemes similar in structure to the adaptive controller here have been used in⁴⁻⁷ for control of fast steering mirrors with significantly different dynamic characteristics from those of the liquid crystal beam steering device here, and in recent papers on adaptive optics⁸⁻¹¹ where many sensor and control channels were used.

Figure 11 illustrates the lattice structure of the FIR filter that generates the adaptive control commands. The lattice realization of an FIR filter of order N consists of N identical stages cascaded as in Fig. 11. The details of the lattice-filter algorithms represented by the blocks in Fig. 11 are beyond the scope of this paper. These algorithms are reparameterized versions of algorithms in.¹² The current parameterization of the lattice algorithms is optimized for indefinite real-time operation. The current lattice filter maintains two important characteristics of the RLS lattice filter in¹²: channel orthogonalization, which is essential to numerical stability in multichannel applications, and the unwindable property (i.e., exact initialization) of the lattice filter, which is essential to rapid convergence.

As indicated in Fig. 11, each stage of the lattice filter generates an adaptive control command. For $n \geq 1$, the output u_n from the n^{th} stage is the optimal control command if an FIR filter of order n is used in the adaptive control loop. For hardware implementation, a maximum filter order N is selected. In each real-time sampling interval, the lattice filter generates the adaptive control commands for all filter orders from 1 to N , and the control algorithm can select which command to use.

Lattice filters are uniquely suited to variable-order adaptive control for the following reason. Because of the order-recursive structure of the lattice filter, computing the control commands for all orders from 1 to N requires no more computation than computing the control command for the order N alone.

The lattice realization of the FIR filter is quite different from the most common FIR realization, which is

$$u_n = \sum_{k=1}^n f_{n,k} z^{1-k} r. \quad (11)$$

While this realization is simpler than the lattice realization, it is less desirable for estimation of optimal gains in adaptive filtering and control. In particular, the optimal gains $f_{n,k}$ for an n^{th} -order FIR filter of the form in (11) are not the first n gains among the optimal gains $f_{N,k}$ for an N^{th} -order FIR filter ($N \geq n$). However, the optimal gains (or reflection coefficients) for the first n stages of the lattice filter are the same for all filter orders $N \geq n$.

Varying the order of the filter in the adaptive controller is important because optimal gains can be identified faster for lower-order filters while higher-order filters are required for optimal steady-state rejection of broadband disturbance. When the adaptive control loop is first closed or when it is adapting to changing disturbance statistics, lower-order control commands should be used initially. The order of the control commands can be increased as the gains for the higher-order filter stages converge. This procedure eliminates large transient responses often produced by initially incorrect gains in high-order filters.

5. EXPERIMENTAL RESULTS

This section presents results from three experiments. In the first experiment, jitter was added by a fast steering mirror (FSM) in the optical path. In the next two experiments, jitter was added by the shaker. In all experiments, building vibration produced additional jitter. In all the experiments, the control loops were closed on both axes. However, because the shaker had minimal effect on the horizontal beam displacement (Axis 1), the result for this axis are not very interesting for the shaker-generated jitter. Hence, only the results for Axis 2 are shown for the last two experiments. For the results presented here, the two components of the output error y measured by the optical position sensor are converted to μrad according to the discussion in Section 4.1.

5.1. Suppression of Jitter Generated by Fast Steering Mirror

The experimental result shown by Fig. 12 exploits the full two dimensional steering capability of the liquid crystal beam steering device. Figure 12 shows the output position errors in the horizontal axis, labeled Axis 1, and the output position errors in the vertical axis, labeled Axis 2. The output position errors with the adaptive loop closed are plotted by the solid blue line and the output errors with the LTI feedback loop closed are plotted by the solid red line. Initially, the LTI feedback control loop is closed, then after approximately 20 seconds the adaptive controller is engaged.

The main source of jitter is generated by driving the Newport Fast Steering Mirror (FSM) with a disturbance sequence d_C , as shown by Fig. 10. The sequence d_C is obtained by passing a white noise sequence through a combination of stable band-pass filters. Although, in experiment, the magnitude of jitter for the two directions was slightly different, the frequency content of the designed jitter was identical in both axes. The jitter description is summarized in Table 1.

The reference signal r for the feedforward adaptive control is the same in each axis,

$$r = d_C. \quad (12)$$

The steady-state RMS values given in Table 2 demonstrate the substantial jitter reduction achieved by the adaptive feedforward controller using the FSM excitation signals. The motivation for using this signal in the feedforward path is to demonstrate the capability of the liquid crystal beam steering device in generating a variety of broad-band signals to compensate for jitters and also evaluate the achievable jitter reduction performance measure. It is conceivable, with good measurements of the disturbance signals, the performance of the entire system can approach this reduction level. The maximum lattice filter order for both channels in this experiment is $N = 16$.

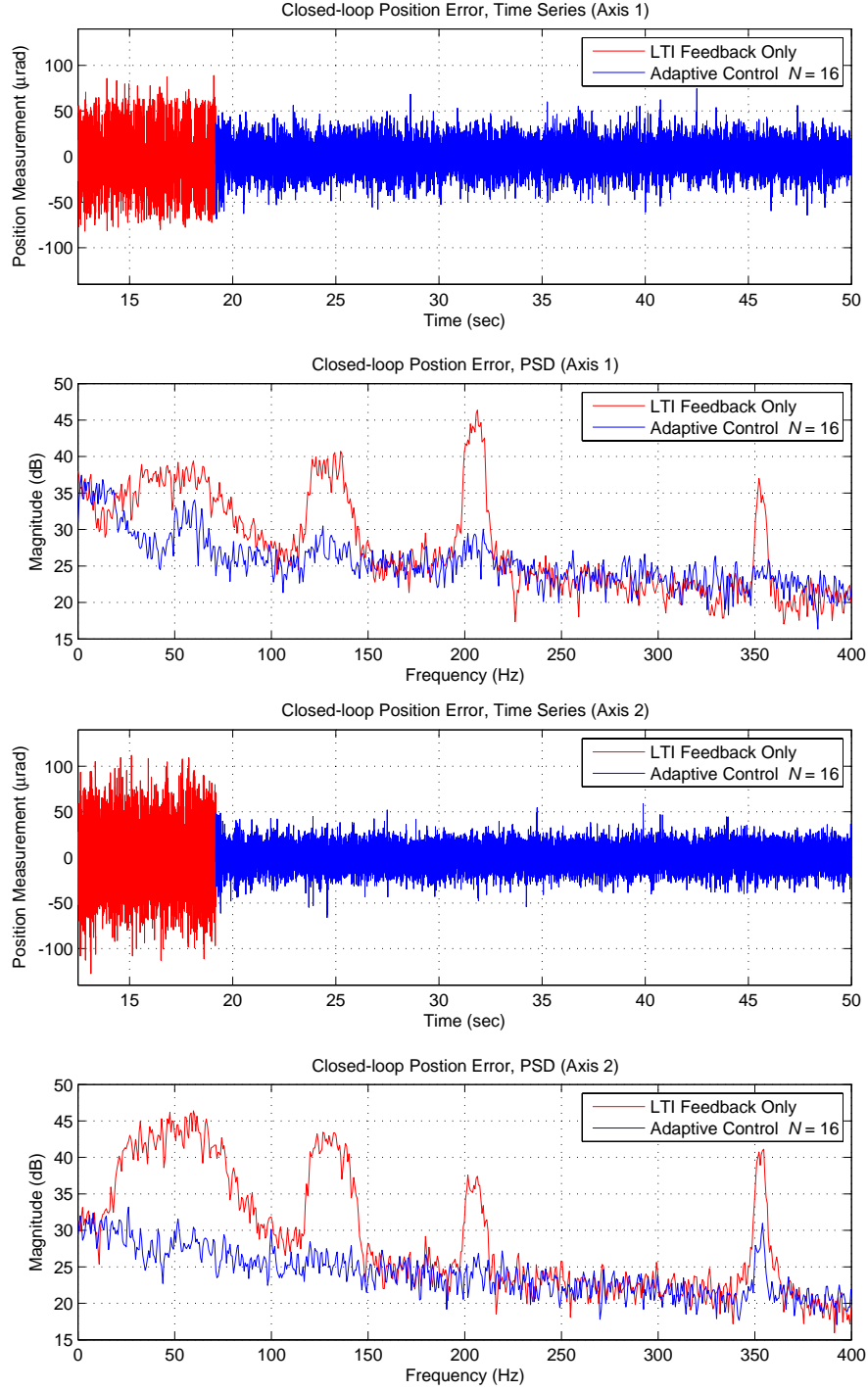


Figure 12. Disturbance rejection performance comparison for the horizontal axis (Axis 1) and the vertical axis (Axis 2). LTI feedback control (red); adaptive control (blue). Maximum lattice filter order $N = 16$. Disturbance sources: fast steering mirror (FSM) and building vibrations (see Table 1). For feedforward adaptive control, reference signal $r = d_C$.

Table 1. Jitter Sources for Axes 1 and Axis 2

Jitter Bandwidths	Source
0 Hz–20 Hz	Misalignments and drift in the optics and response to building vibration d_B
20 Hz–70 Hz pass band	Command d_C to Fast Steering Mirror
120 Hz–140 Hz pass band	Command d_C to Fast Steering Mirror
200 Hz–210 Hz pass band	Command d_C to Fast Steering Mirror
350 Hz–355 Hz pass band	Command d_C to Fast Steering Mirror

Table 2. Steady-state RMS output errors, $r = d_C$

Controller	Axis 1	Axis 2
LTI Feedback Only	23.457 μrad	33.294 μrad
Adaptive Controller, $N = 16$	12.611 μrad	10.111 μrad

5.2. Suppression of Jitter Generated by Shaker

In this section, the main jitter source is generated by the mechanical shaker located beneath the FSM. Experiments with accelerometer signal, which is mounted on top of the FSM, and the shaker driving signal, respectively, will be presented next. The FSM is not subject to the excitation d_C as in the experiment of the previous section. The two main sources of jitter in the experiments are the unintentional ground vibrations d_B and the designed input commands sent to the shaker d_S (see Fig. 4). The sequence d_S is obtained by passing a white noise sequence through a combination of stable band-pass filters with a frequency content given by Table 3.

Table 3. Jitter Sources for Axis 2

Jitter Bandwidths	Source
0 Hz–20 Hz	Misalignments and drift in the optics and response to building vibration d_B
60 Hz–90 Hz pass band	Command d_S to Shaker
120 Hz–140 Hz pass band	Command d_S to Shaker
298 Hz–305 Hz pass band	Command d_S to Shaker

Accelerometer feedforward Figure 13 compares the output angle errors along Axis 2 in an experiment where accelerometer signal is used as the reference signal in the adaptive feedforward control, i.e.

$$r = Ha_M, \quad (13)$$

where H is a digital 8th-order Butterworth band-pass filter with a 55Hz–340Hz pass band and a_M is the accelerometer measurement. The main reason for filtering the measurements is to avoid the unreliable low frequency content given by the accelerometer.

Initially the LTI feedback control loop is closed, then after approximately 20 seconds the adaptive controller is engaged. The output position errors achieved by the LTI feedback loop are plotted by the solid red line and the output position errors of the adaptive loop with the maximum lattice filter order $N = 10$ are plotted by the solid blue line. The PSD plots are calculated from the experimental data for the following time intervals: the LTI feedback loop is based on the 3–18 seconds time range and the adaptive loop is based on the 30–45 seconds time range.

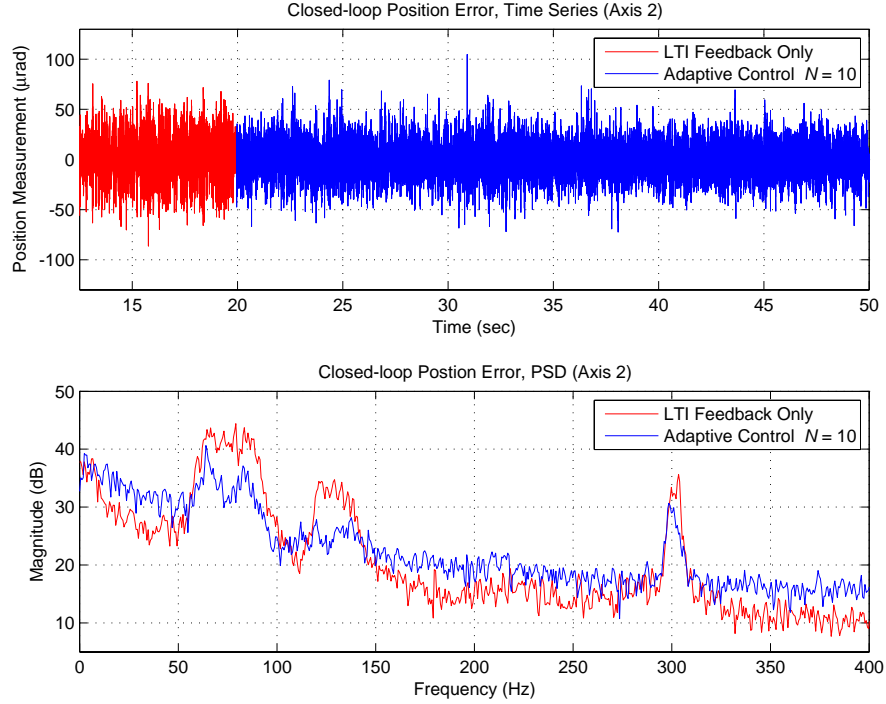


Figure 13. Disturbance rejection performance comparison for the vertical axis (Axis 2). LTI feedback control (red); adaptive control (blue). Maximum lattice filter order $N = 10$. Disturbance sources: shaker and building vibrations (see Table 3). For feedforward adaptive control, reference signal is a filtered accelerometer measurement.

The disturbance rejection improvement achieved by the adaptive controller is more readable from inspecting the PSD plots shown by Fig. 13, where the adaptive loop clearly has various levels of jitter reduction in different pass bands listed in Table 3. Although the jitter reduction in the time series plots are not as evident as in the PSD plots, the comparison of the steady-state RMS values given in Table 4 shows 25% reduction over that of LTI feedback control.

Table 4. Steady-state RMS output errors, $r = Ha_M$

Controller	Axis 2
LTI Feedback Only	19.531 μrad
Adaptive Controller, $N = 10$	14.973 μrad

Jitter-command feedforward The experimental result shown by Fig. 14 differs from the previous experiment in only one aspect. The reference signal used by the adaptive controller is the shaker driving signal, i.e.

$$r = d_S. \quad (14)$$

The maximum lattice filter order, the engagement time of the adaptive loop and the jitter characteristics are

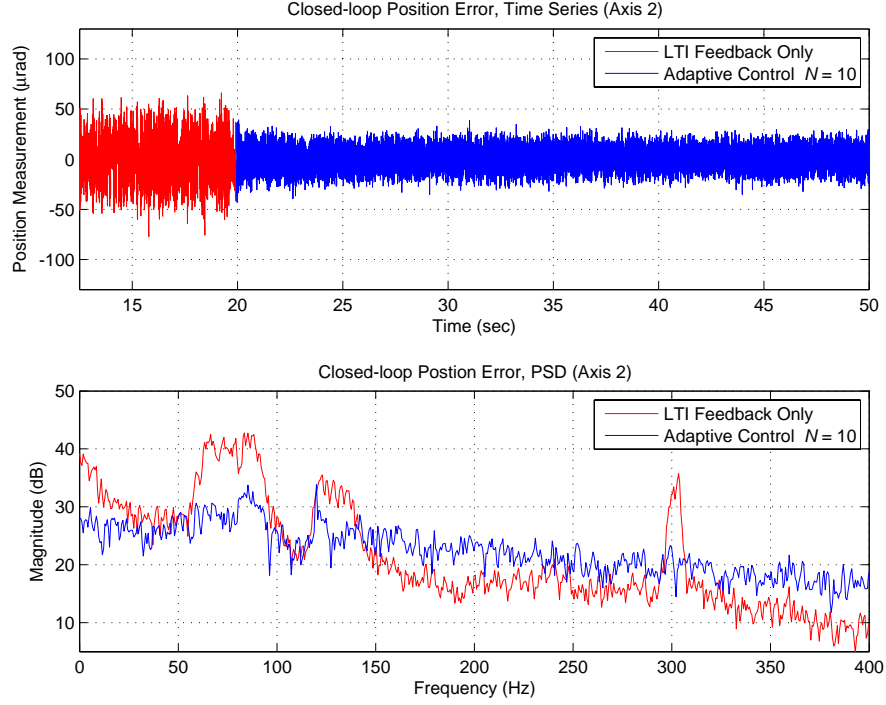


Figure 14. Disturbance rejection performance comparison for the vertical axis (Axis 2). LTI feedback control (red); adaptive control (blue). Maximum lattice filter order $N = 10$. Disturbance sources: shaker and building vibrations (see Table 3). For feedforward adaptive control, reference signal $r = d_S$.

all the same as in the previous experiment shown by Fig. 13. The motivation for constructing the reference signal with (14) is due to the same arguments raised in the previous subsection. The improvement in the second experiment is most apparent in the time series plots shown in Fig. 14. The comparison of the steady-state RMS values is given in Table 5. Furthermore, the PSD plots also illustrate a significant jitter suppression improvement in the low-frequency and the high frequency narrow-band jitter centered at around 300Hz.

Table 5. Steady-state RMS output errors, $r = d_S$

Controller	Axis 2
LTI Feedback Only	18.393 μrad
Adaptive Controller, $N = 10$	8.789 μrad

6. CONCLUSIONS

This paper has demonstrated the use of a new liquid crystal beam steering device for closed-loop control of optical jitter. The liquid crystal beam steering device performs 2-axis beam steering like a fast steering mirror with the

features of 2 μrad resolution over a range of $\pm 300 \mu\text{rad}$, rapid angle transition within its driver's 3125 Hz update rate, and is free of mechanical moving parts and flexures that generate resonances. Both linear time-invariant (LTI) feedback and adaptive feedforward control were applied to drive the liquid crystal beam steering device in synchronization with the driver update rate. The results illustrate that, as in jitter control with mechanical fast steering mirrors,⁴⁻⁷ the jitter-rejection bandwidth is much higher with adaptive control than with LTI feedback. This is particularly noteworthy in the case of the liquid crystal beam steering device because the mapping from the control commands to the output beam angle is somewhat nonlinear due to quantization and a rate limit, whereas the adaptive controller uses a linear model of the liquid crystal beam steering device. The results indicate that the nonlinearities associated with the liquid crystal beam steering device are not sufficiently large to prevent the adaptive controller from compensating for these modeling errors.

The results also show that adaptive feedforward control using direct measurement of disturbance source signals achieves considerably larger jitter suppression than using such indirect disturbance measurement as from accelerometers. Since only indirect measurement using inertial sensors is practically possible in a real application, the quality, dynamics, and location of the inertial sensors are important in order for adaptive feedforward control to achieve similar level of jitter reduction as using the disturbance source signal.

Finally, the adaptive feedforward control scheme can be implemented in two ways in real applications. In the first method, with beam position error measurement available in real time, the adaptive feedforward controller adjusts the filter coefficients to minimize the beam position RMS error with respect to disturbance statistics that could be time varying. In the second method, when the jitter statistical characteristics are stationary but the beam position measurement is not available or adequate for the jitter bandwidth, adaptive feedforward uses a one-time beam position error sensor to tune a feedforward compensator, which is then fixed and deployed in an environment free of beam position sensor. The fixed feedforward compensator should minimize the jitter similarly to the first method as long as the jitter statistics are stationary. With one or the other of these two methods, the adaptive control scheme presented in this paper should be effective in each of the options described in Fig. 1 for tactical line of sight stabilization.

ACKNOWLEDGMENTS

UCLA was supported by the U. S. Air Force Office of Scientific Research under AFOSR Grants F49620-02-01-0319 and F-49620-03-1-0234. The liquid crystal tilt corrector device development was supported by US Air Force (AFRL)/ DARPA ATO contract number FA8650-04-C-7109 and HEL Joint Technology Office project SA05-130. We wish to thank Dr. Bruce Winker at Teledyne Scientific for several enlightening technical discussions.

REFERENCES

1. Yu-Hua Lin, Milind Mahajan, Donald Taber, Bing Wen, and Bruce Winker, "Compact 4 cm aperture transmissive liquid crystal optical phased array for free-space optical communications," **5892**, pp. 58920C1-10, SPIE, August 2005.
2. Dong-Feng Gu, Bruce Winker, Donald Taber, Jeff Cheung, Yiwei Lu, Paul Kobrin, and Zhiming Zhuang, "Dual frequency liquid crystal devices for infrared electro-optical applications," **4799**, pp. 37-47, SPIE, 2002.
3. D. Gu, B. Winker, B. Wen, D. Taber, and A. Brackley, "Wavefront control with a spatial light modulator containing dual-frequency liquid crystal," **5553**, pp. 68-82, SPIE, 2004.
4. Pawel K. Orzechowski, Steve Gibson, and Tsu-Chin Tsao, "Optimal jitter rejection in laser beam steering with variable-order adaptive control," in *Conference on Decision and Control*, IEEE, (San Diego, CA), December 2006.
5. Pawel K. Orzechowski, Steve Gibson, and Tsu-Chin Tsao, "Adaptive control of jitter in a laser beam pointing system," in *American Control Conference*, IEEE, (Minneapolis, MN), June 2006.
6. Néstor O. Pérez Arancibia, Neil Chen, Steve Gibson, and Tsu-Chin Tsao, "Adaptive control of a MEMS steering mirror for suppression of laser beam jitter," in *American Control Conference*, IEEE, (Portland, OR), June 2005.

7. Néstor O. Pérez Arancibia, Neil Chen, Steve Gibson, and Tsu-Chin Tsao, "Adaptive control of a MEMS steering mirror for free-space laser communications," in *Optics and Photonics 2005*, SPIE, (San Diego, CA), August 2005.
8. J. S. Gibson, C.-C. Chang, and B. L. Ellerbroek, "Adaptive optics: wavefront correction by use of adaptive filtering and control," *Applied Optics, Optical Technology and Biomedical Optics* **39**, pp. 2525–2538, June 2000.
9. J. S. Gibson, C.-C. Chang, and Neil Chen, "Adaptive optics with a new modal decomposition of actuator and sensor spaces," in *American Control Conference*, (Arlington, VA), June 2001.
10. Yu-Tai Liu and Steve Gibson, "Adaptive optics with adaptive filtering and control," in *American Control Conference*, IEEE, (Boston, MA), June 2004.
11. Yu-Tai Liu, Neil Chen, and Steve Gibson, "Adaptive filtering and control for wavefront reconstruction and jitter control in adaptive optics," in *American Control Conference*, IEEE, (Portland, OR), June 2005.
12. S.-B. Jiang and J. S. Gibson, "An unwindowed multichannel lattice filter with orthogonal channels," *IEEE Transactions on Signal Processing* **43**, pp. 2831–2842, December 1995.